Estimating marine ice thickness beneath the Amery Ice Shelf from airborne radio-echo sounding

Lijuan Wang[1,2,3,4] iD, Xueyuan Tang[3,5] iD, Jingxue Guo[3] iD, Gang Qiao[1,2],
Lu An[1,2] iD, Lin Li[3], Jamin S. Greenbaum[6], Christina Hulbe[4], Feras A. Habbal[7],
Lenneke M. Jong[8] iD, Tas van Ommen[8] iD, Jason L. Roberts[8], Duncan A. Young[9],
Donald D. Blankenship[9], Bo Sun[3]

[1]Center for Spatial Information Science and Sustainable Development Applications, Tongji University, Shanghai, China; [2]College of Surveying and Geo-Informatics, Tongji University, Shanghai, China; [3]Key Laboratory of Polar Science, MNR, Polar Research Institute of China, Shanghai, China; [4]National School of Surveying, University of Otago, Dunedin, New Zealand; [5]School of Oceanography, Shanghai Jiao Tong University, Shanghai, China; [6]Scripps Institution of Oceanography, University of California, San Diego, La Jolla, CA, USA; [7]Oden Institute for Computational Engineering and Sciences, University of Texas at Austin, Austin, TX, USA; [8]Australian Antarctic Division, Department of Climate Change, Energy, the Environment and Water, Kingston, TAS, Australia and [9]Institute for Geophysics, University of Texas at Austin, Austin, TX, USA

Abstract

Ice shelves affect the stability of ice sheets by supporting the mass balance of ice upstream of the grounding line. Marine ice, formed from supercooled water freezing at the base of ice shelves, contributes to mass gain and affects ice dynamics. Direct measurements of marine ice thickness are rare due to the challenges of borehole drilling. Here we assume hydrostatic equilibrium to estimate marine ice distribution beneath the Amery Ice Shelf (AIS) using meteoric ice-thickness data obtained from radio-echo sounding collected during the Chinese National Antarctic Research Expedition between 2015 and 2019. This is the first mapping of marine ice beneath the AIS in nearly 20 years. Our new estimates of marine ice along two longitudinal bands beneath the northwest AIS are spatially consistent with earlier work but thicker. We also find a marine ice layer exceeding 30 m of thickness in the central ice shelf and patchy refreezing downstream of the grounding line. Thickness differences from prior results may indicate time-variation in basal melting and freezing patterns driven by polynya activity and coastal water intrusions masses under the ice shelf, highlighting that those changes in ice–ocean interaction are impacting ice-shelf stability.

1. Introduction

The Antarctic ice sheet plays a crucial role in global climate processes, and the stability of its ice shelves is considered a major source of uncertainty in predicting future sea level (Hanna and others, 2020; Fox-Kemper and others, 2021). Floating ice shelves occur along 75% of the Antarctic coastline, forming a vital connection between the ice sheet and the ocean (Ingels and others, 2021) and their dynamic changes are critical in assessing the ice sheet mass balance and its contribution to sea level rise (Shepherd and others, 2018). Ice shelves are composed of meteoric ice from two sources, ice flowing from grounded glaciers and the ice sheet and new snow accumulation on the upper surface, together with marine ice formed mainly through the accretion of frazil ice crystals at the ice–ocean interface (Jansen and others, 2013).

Marine ice is the product of thermohaline circulation at the bottom of ice shelves (Robin, 1979), which is driven by the ice pump mechanism (Lewis and Perkin, 1986; Bombosch and Jenkins, 1995) in which cool and relatively fresh water formed by ice melting at depth rises buoyantly toward the shelf front. Ice crystals may form in the rising water where it becomes supercooled as the ambient pressure declines. This supercooled water and the crystals it produces are the sources of marine ice. The accumulation of marine ice alters the thickness of the ice shelf and the bottom structure, reducing the net mass loss of ice shelves and affecting ice flow and circulation at the bottom of the ocean (Williams and others, 2002; Craven and others, 2009). Moreover, marine ice can modulate the stress field and inhibit crack propagation, which impacts the stability of ice shelves (Jansen and others, 2013; Kulessa and others, 2014; Hillebrand and others, 2021; Harrison and others, 2022). Therefore, accurately describing the spatial distribution of bottom marine ice is crucial in dynamically modeling the evolution of ice shelves and assessing their instability.

Marine ice has been detected beneath several ice shelves in Antarctica (Neal, 1979; Thyssen, 1988; Craven and others, 2004; Holland and others, 2009), with the Amery Ice Shelf (AIS), the largest ice shelf in East Antarctica, being one of the key focuses of research. The presence of marine ice under the AIS was first observed in a borehole during a polar expedition in 1968 (Morgan, 1972). Fricker and others (2001) subsequently mapped the distribution of marine ice using satellite laser altimetry, airborne radio-echo sounding (RES) measurements and the hypothesis that differences between RES-observed thickness and thickness predicted using Archimedes' principle and the surface height must be due to an unobserved layer of marine ice. The Australian Amery Ice Shelf Ocean Research (AMISOR) project then investigated the internal structure of the ice shelf and the interaction between the ice base and the ocean through six hot-water-drilled boreholes (AM01–AM06) (Fig. 2; Allison and Craven, 2000; Craven and others, 2014). However, previous inversion or measurement results were constrained by the detection limitations of airborne radar, such as the uncertainties inherent in the early analogue, lower geolocation accuracy and limited depth resolution (Popov, 2022), all of which introduce error in marine ice-thickness estimates. In situ observations are sparse and there have been no follow-up measurements of marine ice thickness on the AIS since Fricker and others' (2001) pioneering work. Meanwhile, global warming has progressed, and changes in polynya formation and ocean circulation on the continental shelf are linked with enhanced ice-shelf melt and delayed formation of dense water (Tamura and others, 2016; Aoki and others, 2022; Jordan and others, 2023; Gu, 2024). A new assessment of the marine ice conditions beneath the ice shelf with contemporary equipment will improve the thickness estimate and improve understanding of AIS processes and change.

Since 2015, the Chinese National Antarctic Research Expedition (CHINARE) has used its 'Snow Eagle 601' fixed-wing airborne platform to conduct a comprehensive suite of aerial observations as part of the ongoing International Collaborative Exploration of the Cryosphere by Airborne Profiling (ICECAP) project. ICECAP observations include gravity, RES and laser altimetry in East Antarctica (e.g. Cui and others, 2020). These observations have yielded the latest physical detection data for the AIS. Yang and others (2021) used ICECAP data to infer seafloor bathymetry and water column thickness under AIS, and explored the potential effects of ice cavity geometry on ocean circulation beneath the ice shelf. Preliminary estimates of marine ice accretion were suggested in two earlier explorations, utilizing the hydrostatic equilibrium method (e.g. Maylath and others, poster presented in AGU Fall Meeting 2018, 2018; https://agu.confex.com/agu/fm18/meetingapp.cgi/Paper/460707). However, these results relied on sparse observational data, and the possible distribution of marine ice was not further investigated.

In this study, we provide a new estimation of the spatial distribution and thickness of marine ice under AIS based on the newly acquired RES data collected during the CHINARE seasons (2015–19). We accomplish this using the surface elevation from satellite observation and the thickness of meteoric ice measured from the above RES data by assuming hydrostatic equilibrium. We then compare the hydrostatic equilibrium results with marine ice-thickness estimates based on the assumption of mass conservation of ice shelves and further estimate the error of the results. Furthermore, we assess the reliability of the results in combination with ice-thickness data obtained from in situ boreholes.

2. Methods and Data

2.1. Hydrostatic equilibrium

For a free-floating ice shelf, a simple relationship between surface elevation h (relative to sea level) and thickness H (Fricker and others, 2001) is given by the hydrostatic equation:

$$h = \frac{\rho_w - \rho_i}{\rho_w} H \qquad (1)$$

where ρ_w and ρ_i are the column-averaged densities of seawater and ice, respectively. In the presence of marine ice accretion at the bottom of the ice shelf, the vertical structure of the ice shelf is composed of an upper layer of meteoric ice and a lower layer of marine ice:

$$H = H_{met} + H_{mar} \qquad (2)$$

in which H_{met} and H_{mar} are the thicknesses of the meteoric and marine ice layers, respectively. As for the upper meteoric ice layer, we use the approach of Fricker and others (2001) to account for the effect of spatial differences in the snow accumulation regime and the temperature structure within the ice layers on column-average density. In this model, the meteoric ice layer is divided into two sub-layers with ρ_{up} and ρ_{low}, respectively. In the horizontal direction, the density model divides the ice shelf into regions characterized by ablation and superimposed ice (between $x = 0$ and 300 m), a region in which the firn layer thickens downstream in a linear manner ($x = 300$–400 m), after which the firn layer reaches an equilibrium thickness. The thickness of the upper sub-layer, h_{up}, is 100 m (Fig. 1; Fricker and others, 2001).

The thickness of the upper meteoric ice layer, H_{met}, can be measured from RES data. The RES data were obtained from aerogeophysical surveys conducted between 2015 and 2019 using the fixed-wing airborne platform 'Snow Eagle 601' operated by the Polar Research Institute of China for the ICECAP project (Fig. 2). The onboard phase-coherent radar system operates at a central frequency of 60 MHz and a bandwidth of 15 MHz, functionally similar to the High Capability Airborne Radar Sounder (HiCARS) developed by the University of Texas Institute for Geophysics (Cui and others, 2018, 2020). Its low center frequency allows for deep ice penetration, while the relatively large bandwidth maintains sufficient resolution to detect key glaciological and geological features. Overall, this system achieves an along-track sampling interval of ∼20 m and a depth resolution of ∼10 m in air and ∼5.6 m in ice. The meteoric-marine ice interface (Moore and others, 1994) or ice–ocean interface (Fig. 3) was picked by Yang and others (2021) using a semiautomatic approach, which first manually bounded the range in which the interface should be found and used an algorithm to extract the brightest return from each trace (Blankenship and others, 2017a,b; Cui and others, 2020). The meteoric ice thickness was calculated by multiplying two-way travel time by the electromagnetic wave speed in ice (0.168 m ns^{-1}; Cui and others, 2018). No firn correction was applied; that is, the thickness includes firn and meteoric ice (Cui and others, 2020). Meteoric ice-thickness data extracted in this way (Yang and others, 2021) is used in the present work (Fig. 2).

However, in locations where basal freezing occurs, the RES data still typically show the bottom of the meteoric ice layer, owing to the high electromagnetic absorption in the marine ice layer (Thyssen, 1988; Lambrecht and others, 2007), which is difficult to penetrate by radar. Thus, where marine ice may be present, there should be a difference between the calculated ice-shelf surface elevation h'
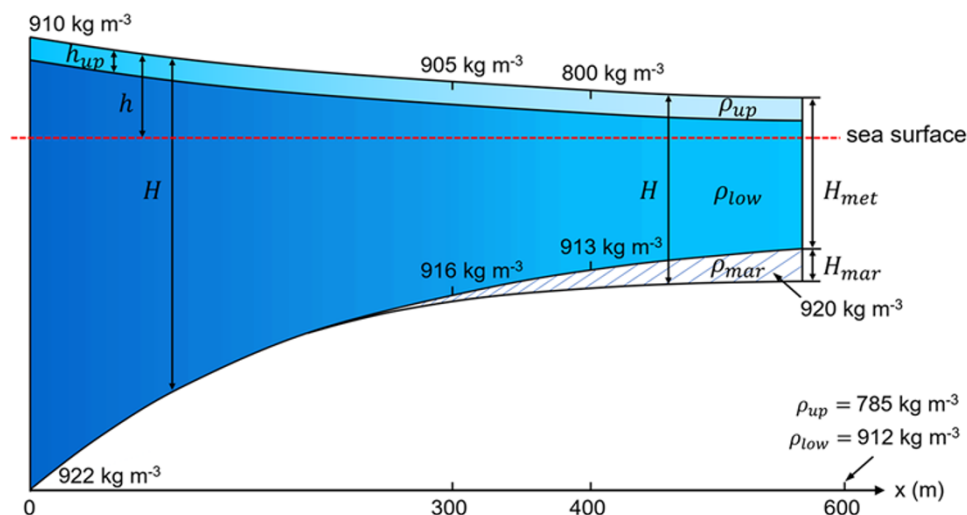
Figure 1. Diagram of a two-layer meteoric ice density model of the ice shelf with values changing linearly along the *x*-direction, with a third layer with a density of 920 kg m^{-3} in areas where marine ice exists. Labels show the ice density at different locations (0, 300, 400 and 600 m from the grounding line).
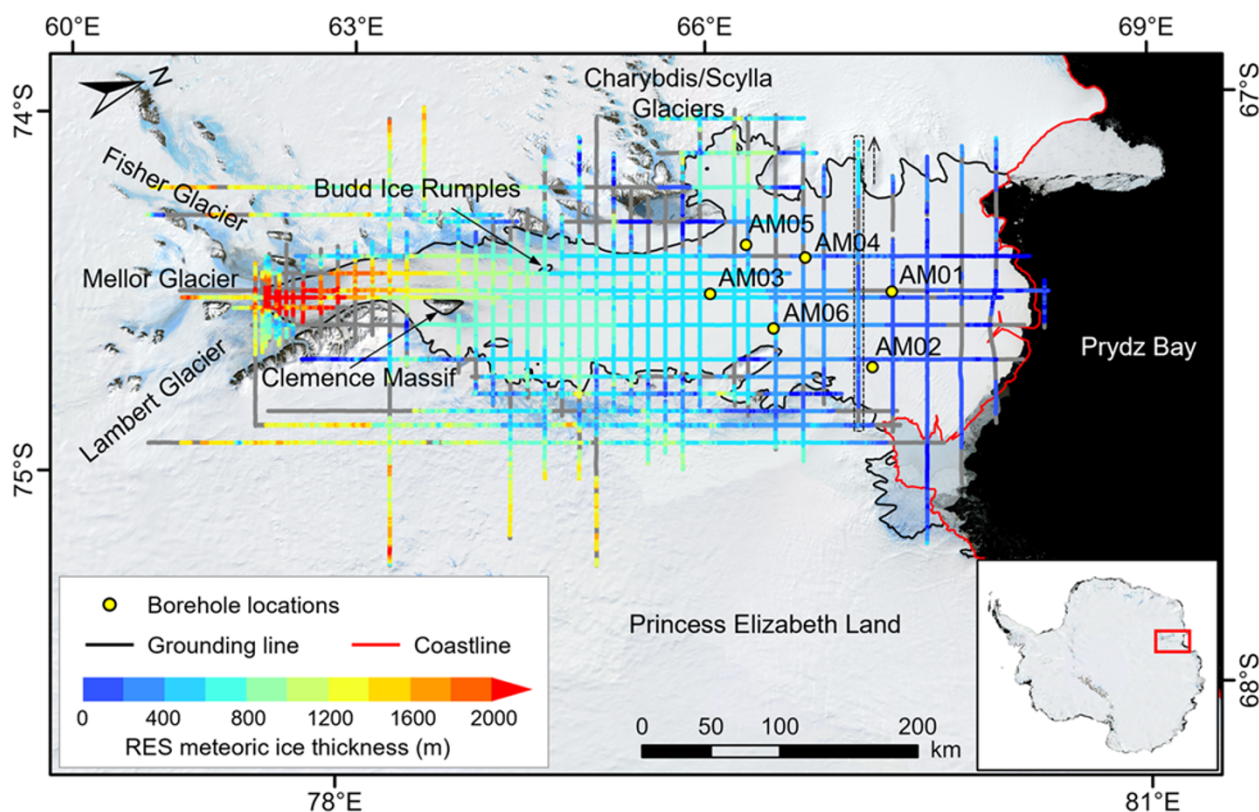

Figure 2. Spatial distribution of meteoric ice thickness extracted from RES data from the ICECAP survey flights (Yang and others, 2021) overlain on the Landsat Image Mosaic of Antarctica (LIMA; Bindschadler and others, 2008). The study area is indicated in the inset. The color bar represents meteoric ice thickness, ranging from 0 m (blue) to 2000 m (red), with missing values shown in gray. The yellow circles indicate the locations of six hot water boreholes in the AMISOR project. The black and red lines denote the grounding line and coastline, respectively, as provided by the dataset of Antarctic boundaries in Table 1 (Mouginot and others, 2017). The dashed box indicates the RES data in Figure 3, and the arrow shows the flight direction.

using H_{met} and the measured surface elevation h, known as the hydrostatic height anomaly:

$$\delta h' = h - h' \qquad (3)$$

Here, h is provided by the Reference Elevation Model of Antarctica (REMA; Howat and others, 2018, 2019). The elevations are from the 200 m-resolution REMA mosaic, acquired between 2011 and 2017 in our study area and are referenced to the mean sea level using the EIGEN-6C4 geoid (Förste and others, 2014). The details of the datasets used here are listed in Table 1. h' is the surface elevation estimated using the meteoric ice thickness from the RES data when no marine ice is assumed to exist. We do not consider
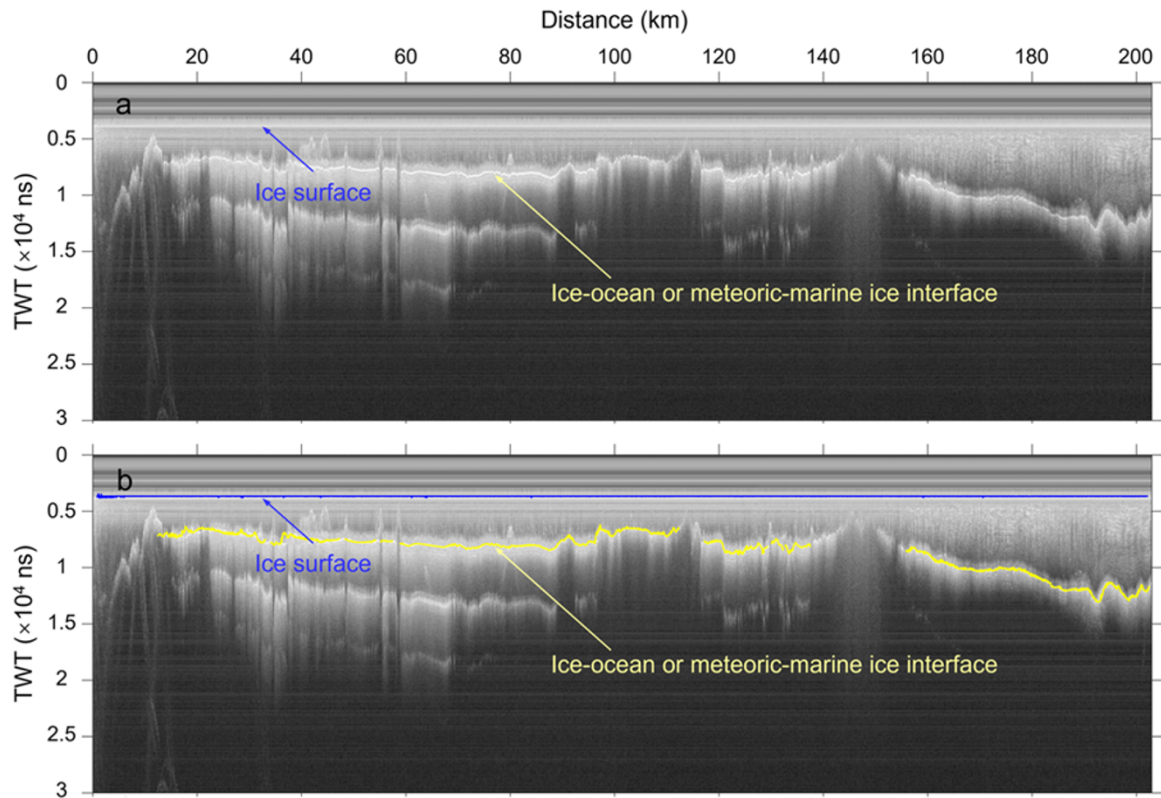
Figure 3. (a) Example of RES data in the dashed box in Figure 2. (b) As (a) with picked interfaces, including the ice-shelf surface (blue line) and the interface of ice–ocean or meteoric-marine ice (yellow line). Between the surface and the bottom is meteoric ice.

Table 1. Datasets used to calculate marine ice thickness

Products	Version	Location	Usage
MEaSUREs Antarctic Boundaries for IPY 2007–2009 from Satellite Radar	Version 2	https://nsidc.org/data/nsidc-0709/versions/2	AIS delineation
High-resolution Image-derived Grounding and Hydrostatic Lines for the Antarctic Ice Sheet	–	http://quantarctica.tpac.org.au/quantarctica/Quantarctica3/Glaciology/ASAID/	Hydrostatic line
Reference Elevation Model of Antarctica (REMA)	Version 1	https://www.pgc.umn.edu/data/rema/	Surface elevation (hydrostatic equilibrium method)
European Improved Gravity Model of the Earth by New Techniques 6C4 (EIGEN-6C4)	EIGEN-6C4	http://icgem.gfz-potsdam.de/home	Geoid (hydrostatic equilibrium method)
MEaSUREs BedMachine Antarctica	Version 2	https://nsidc.org/data/nsidc-0756/versions/2	Ice thickness (mass conservation method)
MEaSUREs InSAR-Based Antarctica Ice Velocity Map	Version 2	https://nsidc.org/data/nsidc-0484/versions/2	Ice velocity (mass conservation method)
Regional Atmospheric Climate Model version 2.3p2 (RACMO2.3p2)	Version 2.3p2	https://www.projects.science.uu.nl/iceclimate/publications/data/2018/index.php	Surface mass balance (mass conservation method)

firn correction in the RES meteoric ice thickness (Cui and others, 2020), which may introduce uncertainty in the thickness measurements. The potential errors resulting from this omission are discussed in Section 3.2. Instead, the column-averaged ice density model with two-layer meteoric ice takes a firn layer into account (Fricker and others, 2001, 2002). Accordingly, we do not apply firn correction to the REMA freeboard when estimating the height anomaly.

The hydrostatic height anomaly is used to identify areas where marine ice may be present. Then, assuming hydrostatic equilibrium and using the three-layer model, the thickness of marine ice can be estimated as

$$H_{mar} = \frac{\rho_w h + (\rho_{up} - \rho_{low}) h_{up} + (\rho_{low} - \rho_w) H_{met}}{\rho_w - \rho_{mar}} \quad (4)$$

in which ρ_{mar} represents the column-averaged density of marine ice, and the other parameters are defined as above. The average density of seawater used in the calculation is 1029 kg m^{-3}, as in Fricker and others (2001). The meteoric ice density is determined as shown in Fig. 1. For marine ice, we use a reference density of 920 kg m^{-3}, which is slightly higher than that of pure ice due to the presence of brines and seawater (Craven and others, 2009). It should be noted that hydrostatic equilibrium may not be valid in the grounding zone of ice shelves (Griggs and Bamber, 2011). Therefore, we

masked the marine ice-thickness map using the hydrostatic line (Bindschadler and others, 2011a,b), and only the results for the free-floating ice shelf are retained.

2.2. Mass conservation

Assuming that the ice shelf is incompressible and always in static equilibrium, the problem of mass conservation can be simplified to the continuity of ice volume (Jenkins and Doake, 1991):

$$\frac{\partial H_i}{\partial t} + \nabla \cdot (H_i V) = \dot{a}_s + \dot{a}_b \qquad (5)$$

in which H_i represents the equivalent thickness of solid ice, V is the horizontal ice velocity, $\dot{a}_s$ is the net surface accumulation rate and $\dot{a}_b$ is the basal accumulation rate. In the context of a steady-state ice shelf, where $\partial H_i / \partial t = 0$, the horizontal divergence in volume flux is balanced by the sum of the surface and basal accumulation rates. Therefore, the basal accumulation rate, $\dot{a}_b$, can be obtained by

$$\dot{a}_b = \nabla \cdot (H_i V) - \dot{a}_s \qquad (6)$$

In the case of floating ice, the shallow-shelf approximation indicates that velocity is constant at all depths and the velocity of meteoric and marine ice is uniform (Sanderson, 1979). Expressing the horizontal ice velocity components along the x and y directions as u and v, respectively, Equation (6) becomes

$$\dot{a}_b = \left[u \frac{\partial H_i}{\partial x} + v \frac{\partial H_i}{\partial y} \right] + \left[(\dot{\varepsilon}_x + \dot{\varepsilon}_y) H_i \right] - \dot{a}_s \qquad (7)$$

in which $\dot{\varepsilon}_x = \partial u / \partial x$ and $\dot{\varepsilon}_y = \partial v / \partial y$ are the corresponding strain rates. To calculate $\dot{a}_b$, we employ two alternative datasets as the solid-ice equivalent thickness H_i: (1) the total thickness of the ice shelf from the hydrostatic equilibrium method (meteoric plus marine ice) with a firn correction applied to obtain ice–equivalent thickness, and (2) the ice-equivalent thickness layer from the BedMachine Antarctica, version 2 dataset (Morlighem, 2020; Morlighem and others, 2020), hereafter referred to as BMA. The BMA provides Antarctic ice thickness and estimation errors at a resolution of 500 m, with most of the ice-shelf area (including AIS) estimated from the early (1994–95) satellite radar altimeter data of the European Remote-sensing Satellite (ERS-1). The horizontal ice velocity data used here is from the MEaSUREs InSAR-based Antarctica Ice Velocity Map, version 2 dataset (Rignot and others, 2017), which provides a digital mosaic of ice motion in Antarctica with a spatial resolution of 450 m derived from multiple satellite radar interferometry data between 1996 and 2016. Considering the random error of the data themselves, the ice thickness and velocity map are smoothed using a circular moving average filter with a 10 km radius before being used to calculate the ice-thickness gradient and strain rate to reduce the noise (Das and others, 2020). The net accumulation rate at the surface is based on the annual surface mass balance (SMB) data simulated by the regional atmospheric climate model version 2.3p2 (RACMO2.3p2; van Wessem and others, 2018) at a spatial resolution of 27 km. For the calculation, the average SMB data from 1996 to 2016 is included as the net surface accumulation rate, given the coverage period of the ice velocity data.

We assume that there is no material conversion process at the interface between meteoric and marine ice, so the thickness of marine ice, H_{mar}, can be derived from Equation (5) using mass conservation (Holland, 2002):

$$\frac{\partial H_{mar}}{\partial t} + \nabla \cdot (H_{mar} V) = \dot{a}_b \qquad (8)$$

Aligning the x-axis with the flow line (Joughin and Vaughan, 2004), the change in H_{mar} can be expressed as

$$\frac{dH_{mar}}{ds} V + \frac{dV}{ds} H_{mar} = \dot{a}_b \qquad (9)$$

in which s represents the distance along the flow line, which is positive along the ice flow. The marine ice thickness is estimated by combing Equations (7) and (9), starting from an initial position where $H_{mar} = 0$, which is the intersection of the flow line and the grounding line. We extract the flow lines based on the MEaSUREs InSAR-based ice velocity, calculate the marine ice thickness on each flow line and obtain a map of marine ice thickness through interpolation.

3. Results

3.1. Marine ice distribution

Our results show two longitudinally distributed marine ice accretion bands to the northwest of the AIS (Fig. 4a), mainly flanking the inflow of Charybdis and Scylla Glaciers, consistent with estimates from previous studies but thicker in some areas (Fricker and others, 2001). In the east of the central ice shelf, located in the middle section of the profile A-A′, we find a thicker layer of marine ice than in previous studies, with a thickness of more than 30 m. In the south, where the ice shelf is relatively thick, we find smaller sites of local freezing distributed along-flow downstream from the grounding line and east of the Budd Ice Rumples. Fricker and others (2001) found a similar pattern of local freezing in this area. It is important to note, however, that the assumption of hydrostatic equilibrium is unlikely to be met everywhere in this region.

The method of mass conservation yields an overall similar spatial pattern as the hydrostatic equilibrium method (Figs 4b and c), but there are some local differences. The mass conservation results using RES are generally thicker, and very high values are produced in the northwest of the two marine ice bands. Causes for differences among the three results are considered in Section 4.

3.2. Error estimation

Uncertainty in the estimated marine ice thickness is quantified by propagating errors associated with measured variables used in Equations (4) and (9). Errors in RES meteoric ice thickness mainly come from observation and the interpolation (Bamber and others, 2013; Chu and others, 2016). Observation errors depend on the precision in range estimates of the radar system and the uncertainty in the time-depth conversion, the latter including the uncertainty in the firn correction and the uncertainty in the electromagnetic wave speed in ice (Cavitte and others, 2016; Winter and others, 2019). Following Luo and others (2022), we use the precision of the range estimates of ±1.63 m for the HiCARS data. Although no firn correction is applied to the data we used, we provide an estimate of the errors caused by using a single electromagnetic wave speed in ice for the time-depth conversion based on the modeled firn air content (obtained from the BMA). Following Sugiyama and others (2010), taking an Antarctic snow dielectric permittivity of 1.644 (corresponding to a speed of 0.234 m ns^{-1}), the estimate will be underestimated by 6 m at the ice front of the AIS where the firn is thickest ($\sim$20 m), which is $\sim$3% of the $\sim$200 m ice thickness there. The electromagnetic wave speed in ice
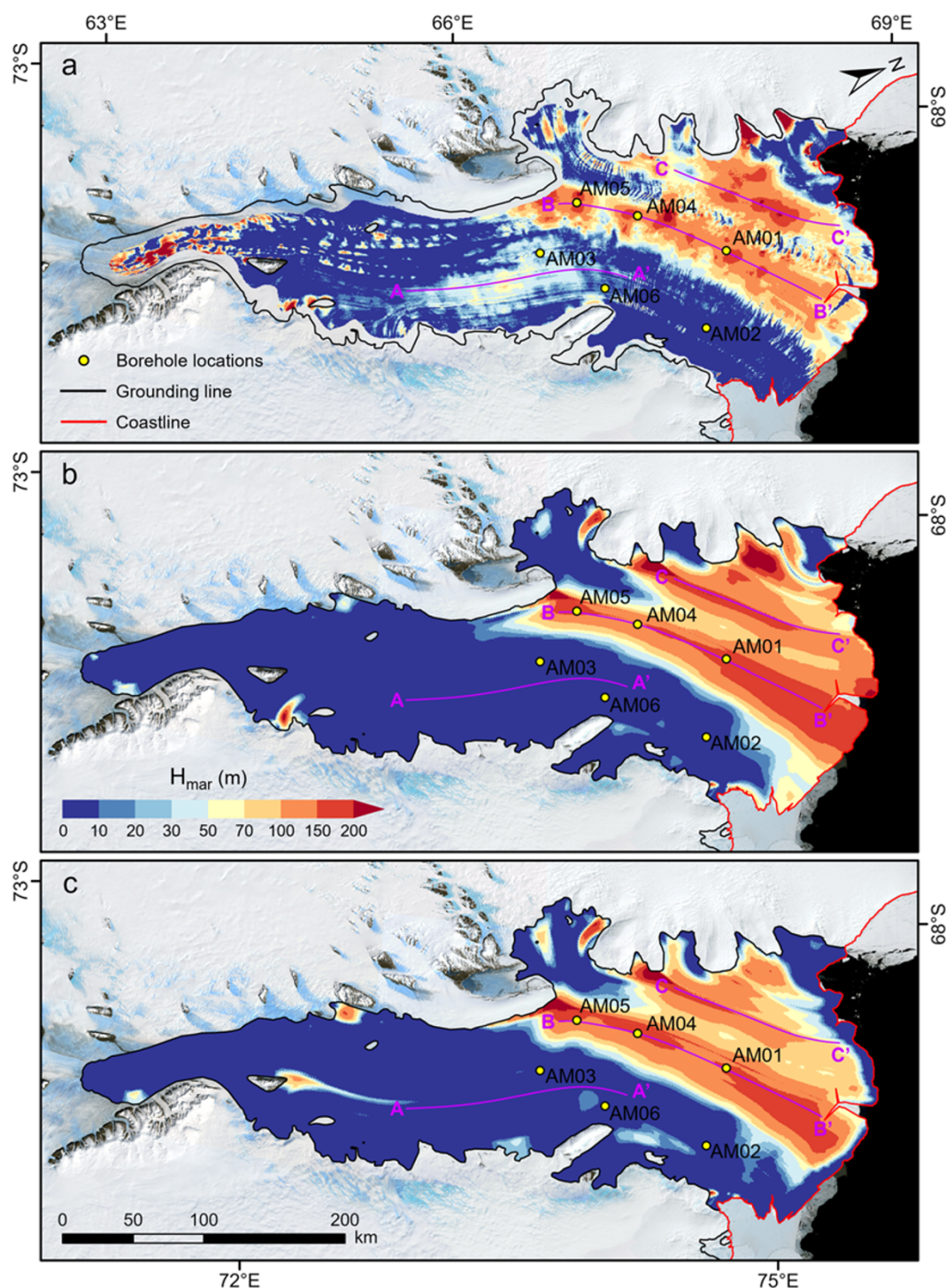
Figure 4. Marine ice distributions beneath the AIS derived from (a) the hydrostatic equilibrium method using RES ice thickness, (b) the mass conservation method using RES ice thickness and (c) the mass conservation method using BMA ice thickness. The yellow circles indicate the locations of six hot water boreholes in the AMISOR project. Purple lines represent the locations of the profiles plotted in Figure 6.

varies from 0.168 to 0.1695 m ns^{-1}, which results in an increasing uncertainty with increased depth (or ice thickness; Fujita and others, 2000; Luo and others, 2022). In our study, the ice thickness of AIS increases from ~200 m at the ice front to ~2500 m at the southern grounding zone; thus, we consider a conservative representation of the uncertainty as ±22 m (within 1% of ice thickness). The uncertainty from the above factors is taken to be ±23 m.

Crossover analysis provides an alternative estimate of the error in the RES meteoric ice-thickness observations. We consider the differences in ice thickness between two measurements at the intersection of two flight lines within 20 m (approximately the along-track spatial sampling rate of the radar system). A total of 189 crossover differences are obtained within the ice shelf, with a standard deviation of ±37 m in ice thickness. This value only
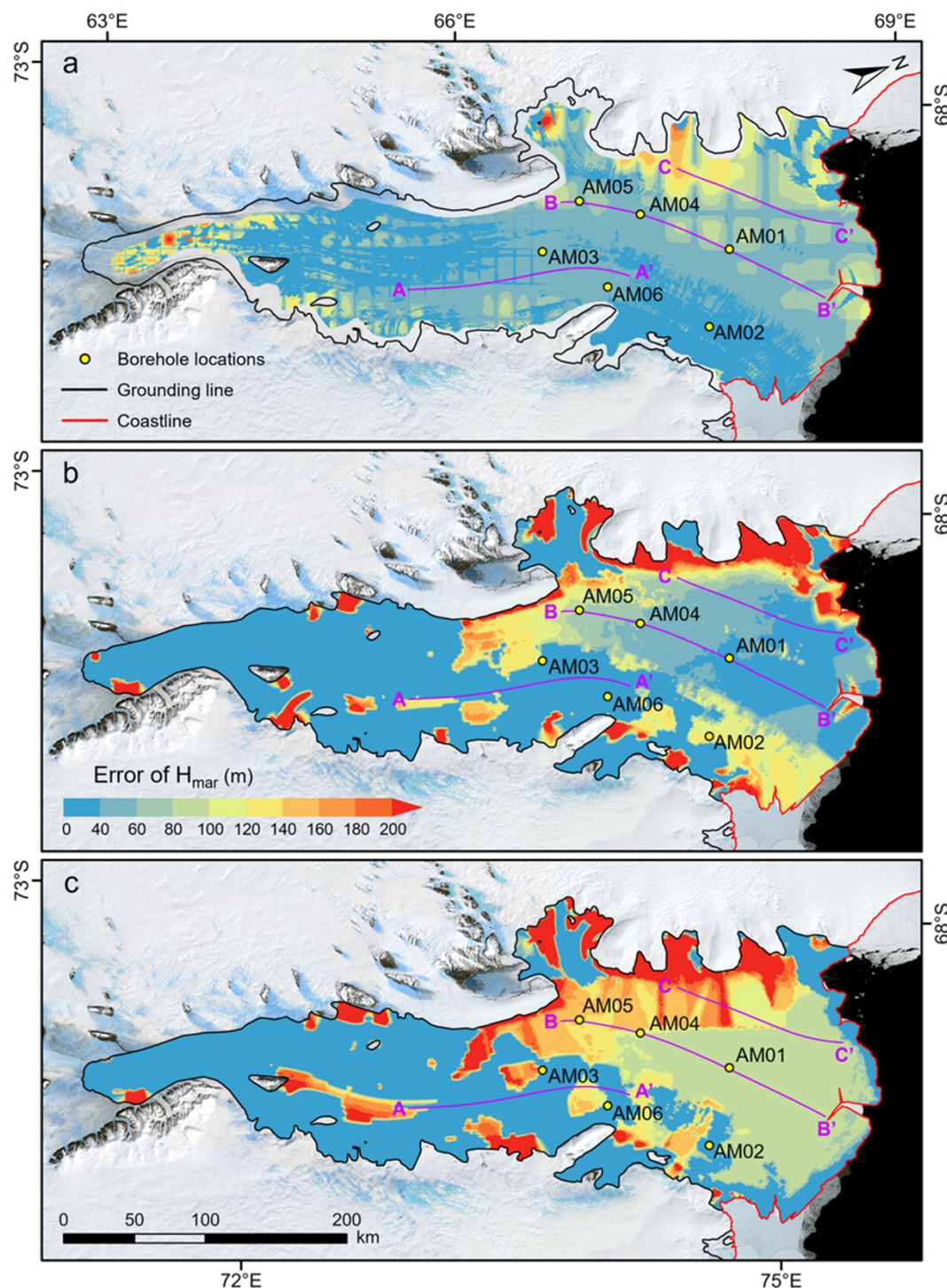
Figure 5. Error maps of marine ice thickness derived from (a) the hydrostatic equilibrium method using RES ice thickness, (b) the mass conservation method using RES ice thickness and (c) the mass conservation method using BMA ice thickness. The yellow circles indicate the locations of six hot water boreholes in the AMISOR project. Purple lines represent the locations of the profiles plotted in Figure 6.

provides the consistency of the data, but we use it in subsequent calculations because it is the more conservative estimate of the error. The interpolation error in the RES meteoric ice thickness depends on the sampling interval of the observations and the variability of the measured ice thickness (Chu and others, 2016). Here, a geostatistical interpolation method, Empirical Bayesian kriging, is used to quantify the uncertainty of the interpolation results by calculating standard errors from a set of predictions generated from multiple semivariograms estimated at each location. We use the Geostatistical Analyst tools provided by ArcGIS to obtain the interpolated ice thickness map from the observed data and the corresponding interpolation error (https://doc.arcgis.com/). Combined with errors in the surface elevation that come from the REMA error (Howat and others, 2018, 2019), we produce a map of the uncertainty in the estimated marine ice thickness (Fig. 5a).

The densities of seawater, meteoric and marine ice are constants applied in our calculations. We use the same values for seawater and meteoric ice as in Fricker and others (2001). The value is slightly higher than the average seawater density directly observed through two of the AMISOR boreholes (1028 kg m^{-3}; Craven and others, 2009). If this seawater density difference were widespread, it would lead us to slightly underestimate the marine ice thickness using the hydrostatic equilibrium method. A difference of 1 kg m^{-3} would result in an underestimation of <8 m in regions of marine ice in the northwest and central ice shelf. The meteoric ice density model may also be a source of bias. The presence of the firn at the surface is accounted for in the two-layer ice density model we used (Fricker and others, 2001, 2002). The average meteoric ice density calculated by Craven and others (2009) using two borehole measurements is within the range applied here following Fricker and others's (2001) two-layer model. However, variations in the density of upper sub-layer meteoric ice (by 1 kg m^{-3}) lead to a difference in the marine ice thickness estimate of <1 m, while variations in the value of the lower sub-layer lead to a difference of <8 m in areas of marine ice, including the northwestern and central regions of the ice shelf. A density of 920 kg m^{-3} is used for marine ice (Craven and others, 2009); however, we note that those authors observe spatial variation related to along-flow diagenesis of the accreted layer. Marine ice layer is expected to be denser where it is younger (and contains more brine), and the sense of the difference would again cause us to overestimate the marine ice thickness in some areas, with a pattern that is likely to be spatially structured. If the density of marine ice was underestimated by 1 kg m^{-3}, the marine ice thickness will be overestimated by <2 m, with this effect occurring in >98% of areas where basal accretion is present. While these calculations provide a sense of scale for the possible error due to the selection of density values used in the calculation, each layer may have a different offset, either positive or negative. A worst case could be overestimates of meteoric ice density (upper and lower) plus underestimates of the densities of marine ice and seawater by 1 kg m^{-3}, in which case the RMS is nearly 12 m. Additionally, changing the upper sub-layer meteoric ice thickness by 1 m will also result in about a 1 m change in the estimated marine ice thickness.

Uncertainty in the mass conservation method is due to errors in ice velocity, solid-ice equivalent thickness and surface accumulation rate. Here, we use the error map that accompanies the ice velocity data product (Rignot and others, 2017) in our calculations. Errors in the solid-ice equivalent thickness are obtained from either the RES ice thickness error or the error estimate provided with the BMA (Morlighem, 2020; Morlighem and others, 2020). Errors in the surface accumulation rate are not reported for RACMO2.3p2 (van Wessem and others, 2018); however, van Wessem and others's (2018) elevation-dependent bias correction is applied.

The hydrostatic equilibrium method using RES data shows the smallest overall uncertainty in marine ice thickness estimation (Fig. 5), indicating its overall better performance compared to the other methods. The equilibrium-method error map is dominated by the uncertainty due to interpolation. Figure 5a shows that the large errors are on the northwest ice shelf (near the profile C-C'), where the interpolation from the sparsity of flight lines leads to larger uncertainty. In addition, the interpolation error is also relatively large near the grounding line, and we attribute this to the undulating terrain here. Uncertainty in the mass conservation method exhibits larger errors near the grounding line on the eastern and western sides of the ice shelf (Figs 5b and c),

primarily arising from uncertainties in the basal accumulation rate. These uncertainties have a greater impact on error propagation because of the relatively small ice flow velocity gradients in these regions.

4. Discussion

4.1. Meteoric ice density model

In this study, the choice of meteoric ice density model plays a crucial role in estimating the marine ice thickness using the hydrostatic equilibrium method. We employ the meteoric ice density model from Fricker and others (2001) to enable effective comparison with their previous work and attempt change detection. This two-layer model represents meteoric ice as an upper and lower layer, each with different column-averaged densities, where the upper layer is set to 100 m thick and accounts for firn air content. While this model provides one way to characterize the meteoric ice density, it is not the only approach. An alternative method involves explicitly separating the firn layer, leading to a different ice density model for the hydrostatic equilibrium method, which we have also considered (Fig. A1 in Appendix A). In this alternative model, the meteoric ice column consists of an upper firn layer and a lower meteoric ice layer. The firn layer thickness is obtained from the BMA, while the lower meteoric ice density follows from Fricker and others (2001). The marine ice thickness estimated using this revised model also shows two longitudinally distributed bands in the northwest of the ice shelf, though the ice thickness is generally thinner than using the two-layer model (Fig. A1a). Additionally, patch basal accretion is observed downstream of the grounding line at the southern end of the ice shelf, whereas no significant accretion is detected east of the central ice shelf. The differences between the two model outputs clearly reveal the spatial pattern of firn layer thickness (Fig. A1c). These findings highlight that the choice of meteoric ice density model can have a dominant impact on hydrostatic equilibrium-based marine ice thickness estimation. It is also important to acknowledge that all meteoric ice density models inherently involve simplifications that influence the final estimates and must be considered when interpreting the results.

4.2. Comparison of marine ice-thickness estimates

While the three results are in broad agreement regarding the spatial pattern of marine ice accumulation on the base of the ice shelf, differences emerge. Three profiles in marine ice accumulation regions show that the differences between the mass conservation and hydrostatic equilibrium estimates generally fall within the uncertainty range of the hydrostatic equilibrium method (Fig. 6). The glaciological contexts and limitations in the observational data explain why some differences emerge. First, the results are in qualitative agreement where velocity gradients are relatively large (profiles B-B' and C-C' in Fig. 6), while they disagree where velocity gradients are smaller (profile A-A' in Fig. 6). The horizontal smoothing inherent in spatial data products appears to reduce the sensitivity of the mass-conservation method. Alley and others (2018) discuss length-scale challenges in their careful analysis of strain-rate estimations. The hydrostatic equilibrium and mass conservation methods also disagree where ice-thickness gradients are large, for example, downstream of the grounding line. Differences along the profile B-B' near 32 km and at the beginning of the profile C-C' are likely due to data gaps, which required interpolation over long distances in some areas. Moreover, the assumption of
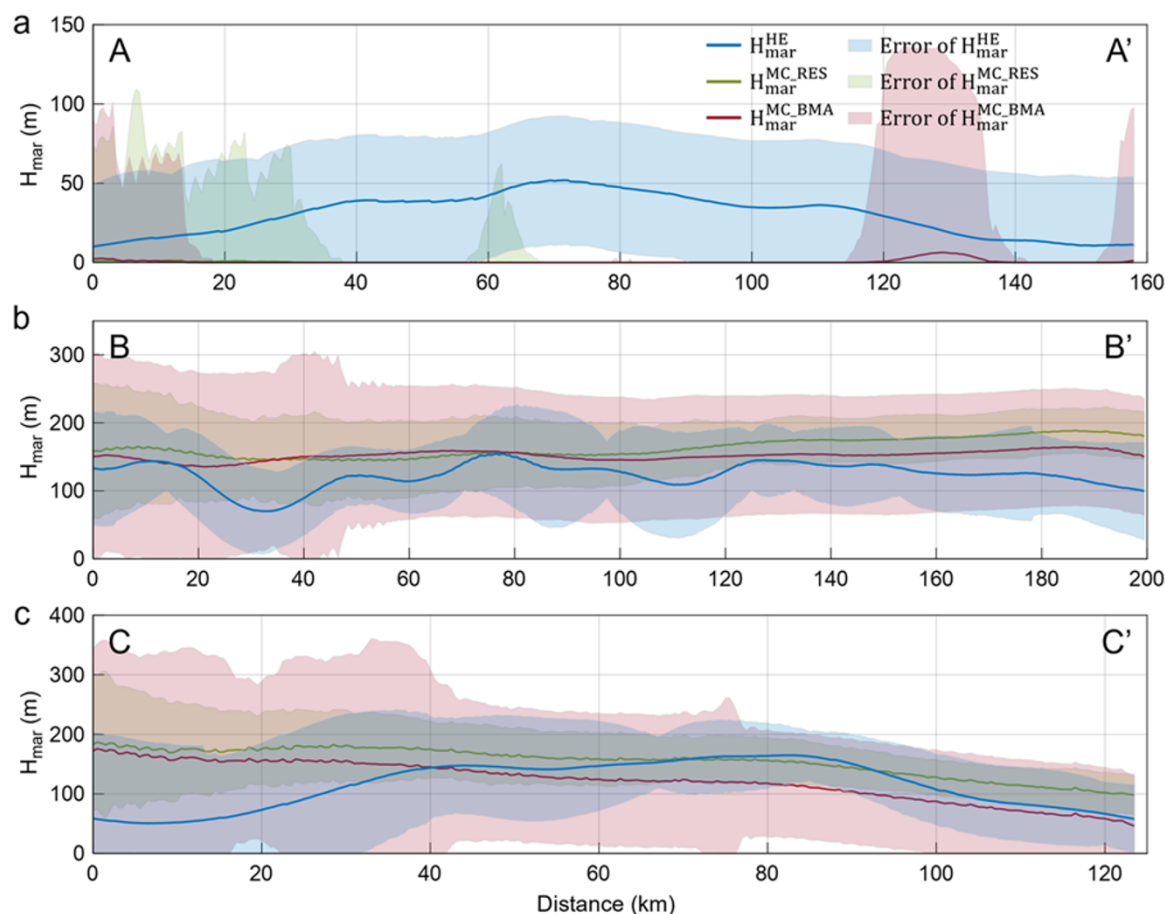
Figure 6. Plots of marine ice thickness and their errors by different methods along profiles (a) A-A', (b) B-B' and (c) C-C' shown in Figures 4 and 5. The blue line shows the hydrostatic equilibrium results from RES data (H_{mar}^{HE}), and the green and red lines represent the mass conservation results from RES ($H_{mar}^{MC\_RES}$) and BMA data ($H_{mar}^{MC\_BMA}$), respectively. The shadings of corresponding colors indicate error ranges. Note that the thickness estimated by the hydrostatic equilibrium method has been smoothed using a circular moving average filter with a 10 km radius to remove noise associated with crevasses and facilitate comparison.

steady state required by the mass conservation method may not be correct, and if not, further complications may arise due to the somewhat different observational epochs represented by different data products. Nevertheless, given the associated uncertainties, the estimated marine ice thicknesses agree reasonably well in most areas of the ice shelf, with differences generally within 50 m (Fig. A2 in Appendix A).

4.3. Comparison with other results

Marine ice thickness was observed directly or inferred from other measurements by the AMISOR project at six hot water borehole sites (Fig. 7; Allison and Craven, 2000; Craven and others, 2014). Both the hydrostatic equilibrium and mass conservation methods yield thinner marine ice than observed at AM01 and AM04 and slightly thicker marine ice than the '>140 m' reported for AM05, which was obtained using fiber-optic temperature (Craven and others, 2014). Both our RES-based hydrostatic result and Fricker and others's (2001) earlier result using the same method indicate thin marine ice layers AM03 and AM06, where no marine ice was observed at the borehole sites. These differences reflect the challenge in comparing point values with maps of fields characterized by large spatial variability as well as uncertainty in the remote-sensing based approaches. Because the various observations were made using data collected over different

time intervals (Table 2), the differences may also reflect changes over time in the ice shelf.

Our new RES-based map of marine ice thickness using the hydrostatic method is broadly similar to the earlier map made using similar data and the same method (Fricker and others, 2001), but differences emerge. First, we find an overall thicker marine ice layer near the calving front, on the order of a few tens of meters. Moving upstream along the flowband containing AM01 to AM05, our estimated ice thickness is similar to the early 1990s estimate in the area around AM01, but we find thicker marine ice upstream from there. Similarly, we find a thicker marine ice layer at and upstream of AM03 and AM06, on the order of a few tens of meters. We also find more widespread marine ice accumulation downstream of the grounding zone than reported by Fricker and others (2001).

4.4. Formation of marine ice

Marine ice thicknesses calculated in this study are generally thicker than estimates made using data spanning the years from 1986 to 1995 (Fricker and others, 2001) and generally closer to thicknesses observed via boreholes between 1999 and 2010. It is possible that the differences between our new results and the older observations represent an increase in basal freezing over time, due to either variability or change in the ice–ocean system. The oceanographic
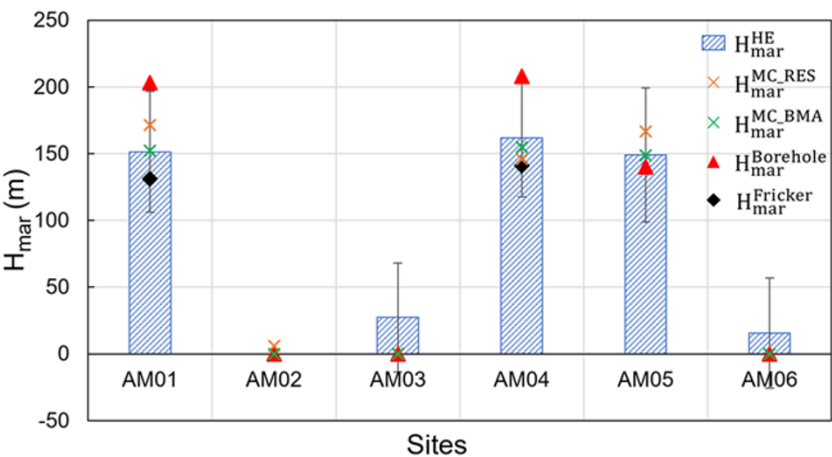
Figure 7. Estimated marine ice thickness of the hydrostatic equilibrium method (H_{mar}^{HE}) with error bars, the estimated results of the mass conservation method ($H_{mar}^{MC\_RES}$ and $H_{mar}^{MC\_BMA}$), the estimates by Fricker and others (2001) ($H_{mar}^{Fricker}$; Craven and others, 2009), and the measurements at boreholes ($H_{mar}^{Borehole}$). Error bars are larger for the mass conservation calculations. Note that the marine ice thickness was not directly measured at AM05, but later inferred to be >140 m from fiber-optic temperature data (Craven and others, 2014).

Table 2. Deployment dates of boreholes in the AMISOR project (Craven and others, 2014) and temporal coverage of the datasets used in earlier studies (Fricker and others, 2001) and this study

AMISOR		Fricker and others (2001)		This study	
Borehole	Deployment date	Dataset	Temporal coverage	Dataset	Temporal coverage
AM01	Jan. 2002	AIS-DEM generated from ERS-1	1994–95	REMA	2011–17
AM02	Jan. 2001	satellite radar altimetry			
AM03	Dec. 2005				
AM04	Jan. 2006	Russian PMGRE RES data	1986–95	CHINARE RES data	2015–19
AM05	Dec. 2009				
AM06	Jan. 2010				
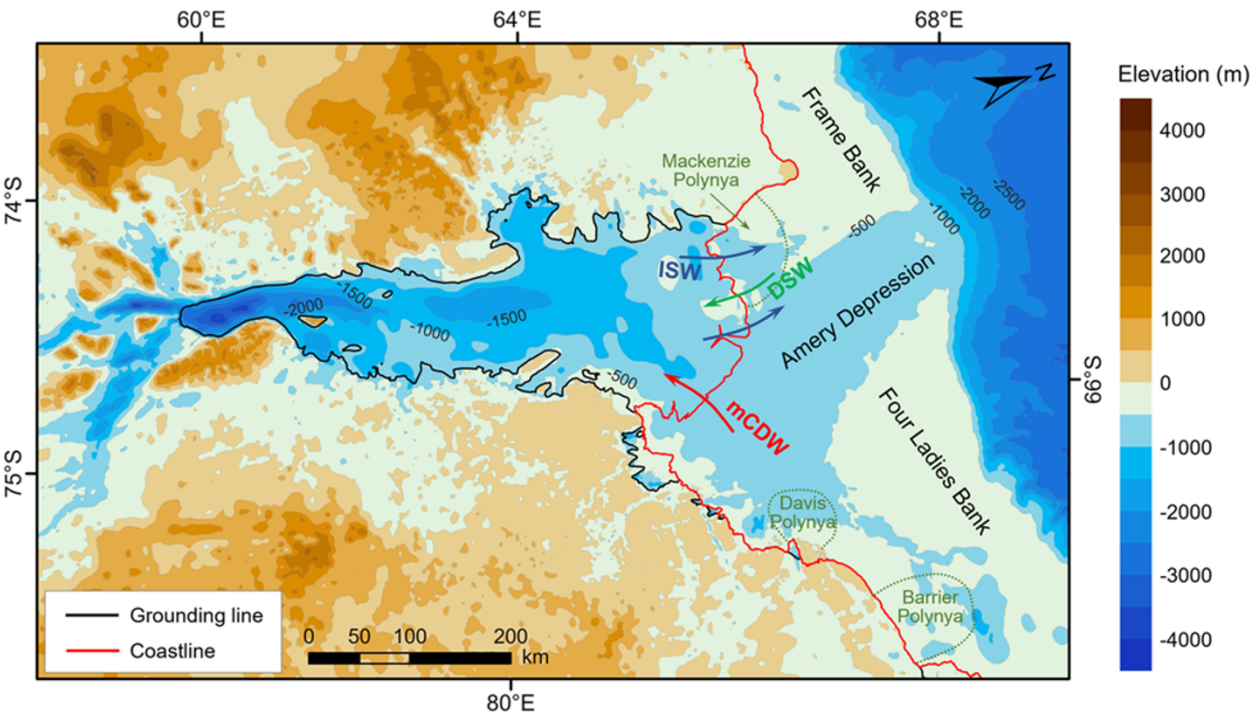
Figure 8. Seafloor topography/bathymetry from Yang and others (2021) beneath the AIS and bed elevation from the Bedmachine Antarctica dataset (outside the AIS). Red and green arrows represent the inflow of mCDW and DSW, respectively, while the blue arrow depicts the outflow of ISW.

processes in Prydz Bay (Fig. 8) play a crucial role in the formation of marine ice, which is primarily driven by two water masses: Dense Shelf Water (DSW), which forms in coastal polynyas and sinks into the cavity under the western flank of the ice shelf, and modified Circumpolar Deep Water (mCDW) inflow on the eastern flank (Herraiz-Borreguero and others, 2015, 2016). The two inflowing water masses produce two distinct types of Ice Shelf Water (ISW), with ISW formed from DSW observed to flow out from the AIS

cavity along the western flank, where marine ice is observed to form (Fricker and others, 2001; Herraiz-Borreguero and others, 2015; Wang and others, 2023).

Time series observations from the AMISOR project show that seasonal DSW intrusion under the ice shelf changes the water column stratification by tilting isopycnal surfaces, raising ISW toward the shelf base and forming frazil ice (Herraiz-Borreguero and others, 2013). Given that marine ice formation is closely linked to ISW supply, either a change in ISW production rate or a change in the timing or intensity of DSW intrusion under the AIS could account for an increase in the amount of marine ice. This, in turn, could be due to variability in polynya activity and DSW production on the shelf (Tamura and others, 2016; Gu, 2024). Additionally, the Prydz Bay Gyre and the Eastern Coastal Current transport mCDW from the eastern side of AIS to the shelf bottom (Smith and others, 1984; Wong and others, 1998; Liu and others, 2017). Variability or change in mCDW circulation under the shelf could also be a source of increased ISW, and in turn, more marine ice formation.

Both the present study and the earlier estimates of Fricker and others (2001) predict the patchy occurrence of marine ice downstream of the AIS grounding line, east of the Budd Ice Rumples, and south of the Clemence Massif. Altimetry-derived estimates of basal melt rates in Adusumilli and others (2020) identify localized freezing near the grounding line, in line with our results, though in a more restricted area than we find. Ocean models (Galton-Fenzi and others, 2012) predict freezing east of the ice rumples but strong melting elsewhere in this region. The apparent contradiction may be explained if some of the cold meltwater formed in this area was rising and refreezing in basal crevasses. Refreezing in basal crevasses downstream of the grounding line was also recently observed downstream of the Kamb Ice Stream grounding line (Lawrence and others, 2023). It is worth noting that the assumption of hydrostatic equilibrium may not always hold near the grounding line, and for this reason, we excluded ice between the grounding line and the hydrostatic line (Bindschadler and others, 2011a,b) in our calculations. The propagated errors are relatively high close to the grounding line (Fig. 5a), nevertheless, even when accounting for these uncertainties in the estimated marine ice-thickness map, the localized refreezing downstream of the grounding line remains non-negligible.

5. Conclusions

Marine ice contributes to the stability of Antarctic ice shelves. In this study, we have provided a new estimate of the spatial distribution and thickness of marine ice underneath the AIS using meteoric ice thickness extracted from RES data collected during the CHINARE seasons (2015–19) for the ICECAP project. Our results show the distribution of two longitudinal marine ice accretion bands in the northwest of AIS, which we conclude to have thickened between our observations and the earlier RES observation campaign. Changes in DSW production on the continental shelf associated with polynya variability are the likely source of such change. We also report accretions of marine ice in the central ice shelf and downstream of the grounding line, areas that have not been a focus of past studies. Our analysis also demonstrates the large errors associated with remote estimation of marine ice thickness and points to the need for more extensive in situ measurements of ice shelves to more accurately assess the ice-shelf structure and monitor interaction processes between the ice shelf and the ocean. Furthermore, the impact of ice accretion at the bottom on ice dynamics and stability of ice shelves remains to

be investigated. Overall, this study contributes to a better understanding of ice–ocean interaction and the stability of Antarctic ice shelves.

References

Adusumilli S, Fricker HA, Medley B, Padman L and Siegfried MR (2020) Interannual variations in meltwater input to the Southern Ocean from Antarctic ice shelves. *Nature Geoscience* **13**, 616–620. doi:10.1038/s41561-020-0616-z

Alley KE, Scambos TA, Anderson RS, Rajaram H, Pope A and Haran TM (2018) Continent-wide estimates of Antarctic strain rates from Landsat 8-derived velocity grids. *Journal of Glaciology* **64**(244), 321–332. doi:10.1017/jog.2018.23

Allison I and Craven M (2000) Ice shelf-ocean interaction in the cavity beneath the Amery Ice Shelf, Ver. 1. *Australian Antarctic Data Centre.* https://data.aad.gov.au/metadata/records/ASAC_1164 (accessed 5 May 2025).

Aoki S and 7 others (2022) Warm surface waters increase Antarctic ice shelf melt and delay dense water formation. *Communications Earth and Environment* **3**(1), 142. doi:10.1038/s43247-022-00456-z

Bamber JL and 10 others (2013) A new bed elevation dataset for Greenland. *Cryosphere* **7**, 499–510. doi:10.5194/tc-7-499-2013

Bindschadler R and 8 others (2008) The Landsat Image Mosaic of Antarctica. *Remote Sensing of Environment* **112**(12), 4214–4226. doi:10.1016/j.rse.2008.07.006

Bindschadler R and 17 others (2011a) Getting around Antarctica: New high-resolution mappings of the grounded and freely-floating boundaries of the Antarctic ice sheet created for the International Polar Year. *Cryosphere* **5**(3), 569–588. doi:10.5194/tc-5-569-2011

Bindschadler R, Choi H and Collaborators ASAID (2011b) *High-resolution Image-derived Grounding and Hydrostatic Lines for the Antarctic Ice Sheet.* *Boulder Colorado, USA*: National Snow and Ice Data Center. Digital media.

Blankenship DD and 12 others (2017a) *IceBridge HiCARS 1 L2 Geolocated Ice Thickness, Version 1*. Boulder, Colorado USA. NASA National Snow and Ice Data Center Distributed Active Archive Center. doi:10.5067/F5FGUT9F5089

Blankenship DD and 12 others (2017b) *IceBridge HiCARS 2 L2 Geolocated Ice Thickness, Version 1*. Boulder, Colorado, USA, NASA National Snow and Ice Data Center Distributed Active Archive Center. doi:10.5067/9EBR2T0VXUDG

Bombosch A and Jenkins A (1995) Modeling the formation and deposition of frazil ice beneath Filchner-Ronne Ice Shelf. *Journal of Geophysical Research* **100**(C4), 6983–6992. doi:10.1029/94JC03224

Cavitte MGP and 7 others (2016) Deep radiostratigraphy of the East Antarctic plateau: Connecting the Dome C and Vostok ice core sites. *Journal of Glaciology* **62**(232), 323–334. doi:10.1017/jog.2016.11

Chu W, Creyts TT and Bell RE (2016) Rerouting of subglacial water flow between neighboring glaciers in West Greenland. *Journal of Geophysical Research: Earth Surface* **121**, 925–938. doi:10.1002/2015JF003705

Craven M and 6 others (2004) Initial borehole results from the Amery Ice Shelf hot-water drilling project. *Annals of Glaciology* **39**, 531–539. doi:10.3189/172756404781814311

Craven M, Allison I, Fricker HA and Warner AR (2009) Properties of a marine ice layer under the Amery Ice Shelf, East Antarctica. *Journal of Glaciology* **55**(192), 717–728. doi:10.3189/002214309789470941

Craven M, Warner RC, Galton-Fenzi BK, Herraiz-Borreguero L, Vogel SW and Allison I (2014) Platelet ice attachment to instrument strings beneath the Amery Ice Shelf, East Antarctica. *Journal of Glaciology* **60**(220), 383–393. doi:10.3189/2014JoG13J082

Cui X and 7 others (2018) The first fixed-wing aircraft for Chinese Antarctic expeditions: Airframe, modifications, scientific instrumentation and applications. *Journal of Environmental and Engineering Geophysics* **23**(1), 1–13. doi:10.2113/JEEG23.1.1

Cui X and 15 others (2020) Bed topography of Princess Elizabeth Land in East Antarctica. *Earth System Science Data* **12**(4), 2765–2774. doi:10.5194/essd-12-2765-2020

Das I and 11 others (2020) Multidecadal basal melt rates and structure of the Ross Ice Shelf, Antarctica, using airborne ice penetrating radar. *Journal of Geophysical Research: Earth Surface* **125**(3), e2019JF005241. doi:10.1029/2019JF005241

Förste C and 10 others (2014) EIGEN-6C4 - The latest combined global gravity field model including GOCE data up to degree and order 2190 of GFZ Postdam and GRGS Toulouse. *GFZ Data Services*. doi:10.5880/icgem.2015.1

Fox-Kemper B and 17 others (2021) *Ocean, Cryosphere and Sea Level Change. In Climate Change 2021: The Physical Science Basis. Contribution of Working Group I to the Sixth Assessment Report of the Intergovernmental Panel on Climate Change*. Cambridge University Press, Cambridge, United Kingdom and New York, NY, USA. doi:10.1017/9781009157896.011

Fricker HA and 9 others (2002) Redefinition of the Amery Ice Shelf, East Antarctica, grounding zone. *Journal of Geophysical Research* **107**(B5), 2092. doi:10.1029/2001JB000383

Fricker HA, Popov S, Allison I and Young N (2001) Distribution of marine ice beneath the Amery Ice Shelf. *Geophysical Research Letters* **28**(11), 2241–2244. doi:10.1029/2000GL012461

Fujita S, Matsuoka T, Ishida T, Matsuoka K and Mae S (2000) A summary of the complex dielectric permittivity of ice in the megahertz range and its applications for radar sounding of polar ice sheets. *Physics of Ice Core Records*, 185–212. http://hdl.handle.net/2115/32469 (accessed 5 May 2025).

Galton-Fenzi BK, Hunter JR, Coleman R, Marsland SJ and Warner RC (2012) Modeling the basal melting and marine ice accretion of the Amery Ice Shelf. *Journal of Geophysical Research: Oceans* **117**(9), C09031. doi:10.1029/2012JC008214

Griggs JA and Bamber JL (2011) Antarctic ice-shelf thickness from satellite radar altimetry. *Journal of Glaciology* **57**(203), 485–498. doi:10.3189/002214311796905659

Gu M (2024) Time series analysis of sea ice production in polynyas in the Amery Ice Shelf in Antarctica. *Environmental Sciences Proceedings* **29**(1), 42. doi:10.3390/ecrs2023-16368

Hanna E and 10 others (2020) Mass balance of the ice sheets and glaciers – Progress since AR5 and challenges. *Earth-Science Reviews* **201**, 102976. doi:10.1016/j.earscirev.2019.102976

Harrison LC, Holland PR, Heywood KJ, Nicholls KW and Brisbourne AM (2022) Sensitivity of melting, freezing and marine ice beneath Larsen C Ice Shelf to changes in ocean forcing. *Geophysical Research Letters* **49**, e2021GL096914. doi:10.1029/2021GL096914

Herraiz-Borreguero L, Allison I, Craven M, Nicholls KW and Rosenberg MA (2013) Ice shelf/ocean interactions under the Amery Ice Shelf: Seasonal variability and its effect on marine ice formation. *Journal of Geophysical Research: Oceans* **118**(12), 7117–7131. doi:10.1002/2013JC009158

Herraiz-Borreguero L and 6 others (2016) Basal melt, seasonal water mass transformation, ocean current variability, and deep convection processes along the Amery Ice Shelf calving front, East Antarctica. *Journal of Geophysical Research: Oceans* **121**(7), 4946–4965. doi:10.1002/2016JC011858

Herraiz-Borreguero L, Coleman R, Allison I, Rintoul SR, Craven M and Williams GD (2015) Circulation of modified Circumpolar Deep Water and basal melt beneath the Amery Ice Shelf, East Antarctica. *Journal of Geophysical Research: Oceans* **120**, 3098–3112. doi:10.1002/2015JC010697

Hillebrand TR, Conway H, Koutnik M, Martín C, Paden J and Winberry JP (2021) Radio-echo sounding and waveform modeling reveal abundant marine ice in former rifts and basal crevasses within Crary Ice Rise, Antarctica. *Journal of Glaciology* **67**(264), 641–652. doi:10.1017/jog.2021.17

Holland DM (2002) Computing marine-ice thickness at an ice-shelf base. *Journal of Glaciology* **48**(160), 9–19. doi:10.3189/172756502781831674

Holland PR, Corr HFJ, Vaughan DG, Jenkins A and Skvarca P (2009) Marine ice in Larsen Ice Shelf. *Geophysical Research Letters* **36**(11), L11604. doi:10.1029/2009GL038162

Howat I, Morin P, Porter C and Noh M-J (2018) The Reference Elevation Model of Antarctica, Version 1. *Harvard Dataverse*. doi:10.7910/DVN/SAIK8B

Howat IM, Porter C, Smith BE, Noh MJ and Morin P (2019) The reference elevation model of Antarctica. *The Cryosphere* **13**(2), 665–674. doi:10.5194/tc-13-665-2019

Ingels J and 38 others (2021) Antarctic ecosystem responses following ice-shelf collapse and iceberg calving: Science review and future research. *Wiley Interdisciplinary Reviews: Climate Change* **12**(1), e682. doi:10.1002/wcc.682

Jansen D, Luckman A, Kulessa B, Holland PR and King EC (2013) Marine ice formation in a suture zone on the Larsen C Ice Shelf and its influence on ice shelf dynamics. *Journal of Geophysical Research: Earth Surface* **118**(3), 1628–1640. doi:10.1002/jgrf.20120

Jenkins A and Doake CSM (1991) Ice-ocean interaction on Ronne Ice Shelf, Antarctica. *Journal of Geophysical Research* **96**(C1), 791–813. doi:10.1029/90JC01952

Jordan JR, Gudmundsson GH, Jenkins A, Stokes CR, Miles BWJ and Jamieson SSR (2023) Increased warm water intrusions could cause mass loss in East Antarctica within 200 years. *Nature Communications* **14**, 1825. doi:10.1038/s41467-023-37553-2

Joughin I and Vaughan DG (2004) Marine ice beneath the Filchner-Ronne Ice Shelf, Antarctica: A comparison of estimated thickness distributions. *Annals of Glaciology* **39**, 511–517. doi:10.3189/172756404781814717

Kulessa B, Jansen D, Luckman AJ, King EC and Sammonds PR (2014) Marine ice regulates the future stability of a large Antarctic ice shelf. *Nature Communications* **5**, 3707. doi:10.1038/ncomms4707

Lambrecht A, Sandhäger H, Vaughan DG and Mayer C (2007) New ice thickness maps of Filchner-Ronne Ice Shelf, Antarctica, with specific focus on grounding lines and marine ice. *Antarctic Science* **19**(4), 521–532. doi:10.1017/S0954102007000661

Lawrence JD and 15 others (2023) Crevasse refreezing and signatures of retreat observed at Kamb Ice Stream grounding zone. *Nature Geoscience* **16**, 238–243. doi:10.1038/s41561-023-01129-y

Lewis EL and Perkin RG (1986) Ice pumps and their rates. *Journal of Geophysical Research* **91**(C10), 11756–11762. doi:10.1029/jc091ic10p11756

Liu C, Wang Z, Cheng C, Xia R, Li B and Xie Z (2017) Modeling modified Circumpolar Deep Water intrusions onto the Prydz Bay continental shelf, East Antarctica. *Journal of Geophysical Research: Oceans* **122**(7), 5198–5217. doi:10.1002/2016JC012336

Luo K and 6 others (2022) Deep radiostratigraphy constraints support the presence of persistent wind scouring behavior for more than 100 Ka in the East Antarctic ice sheet. *IEEE Transactions on Geoscience and Remote Sensing* **60**, 1–13. doi:10.1109/TGRS.2022.3209543

Moore JC, Reid AP and Kipfstuhl J (1994) Microstructure and electrical properties of marine ice and its relationship to meteoric ice and sea ice. *Journal of Geophysical Research* **99**(C3), 5171–5180. doi:10.1029/93JC02832

Morgan VI (1972) Oxygen isotope evidence for bottom freezing on the Amery Ice Shelf. *Nature* **238**, 393–394. doi:10.1038/238393a0

Morlighem M (2020) *MEaSUREs BedMachine Antarctica, Version 2.* Boulder, Colorado USA. NASA National Snow and Ice Data Center Distributed Active Archive Center. doi:10.5067/E1QL9HFQ7A8M

Morlighem M and 36 others (2020) Deep glacial troughs and stabilizing ridges unveiled beneath the margins of the Antarctic ice sheet. *Nature Geoscience* **13**(2), 132–137. doi:10.1038/s41561-019-0510-8

Mouginot J, Scheuchl B and Rignot E (2017) *MEaSUREs Antarctic Boundaries for IPY 2007-2009 from Satellite Radar, Version 2.* Boulder, Colorado USA. NASA National Snow and Ice Data Center Distributed Active Archive Center. doi:10.5067/AXE4121732AD

Neal CS (1979) The dynamics of the Ross Ice Shelf revealed by radio echo-sounding. *Journal of Glaciology* **24**(90), 295–307. doi:10.1017/S0022143000014817

Popov S (2022) Ice cover, subglacial landscape, and estimation of bottom melting of Mac. Robertson, Princess Elizabeth, Wilhelm II, and Western Queen Mary Lands, East Antarctica. *Remote Sensing* **14**(1), 241. doi:10.3390/rs14010241

Rignot E, Mouginot J and Scheuchl B (2017) *MEaSUREs InSAR-Based Antarctica Ice Velocity Map, Version 2.* Boulder, Colorado USA. NASA National Snow and Ice Data Center Distributed Active Archive Center. doi:10.5067/D7GK8F5J8M8R

Robin GD (1979) Formation, flow, and disintegration of ice shelves. *Journal of Glaciology* **24**(90), 259–271. doi:10.3189/s0022143000014787

Sanderson TJO (1979) Equilibrium profile of ice shelves. *Journal of Glaciology* **22**(88), 435–460. doi:10.3189/S0022143000014453

Shepherd A and 79 others (2018) Mass balance of the Antarctic Ice Sheet from 1992 to 2017. *Nature* **558**, 219–222. doi:10.1017/cbo9780511535659.014

Smith NR, Zhaoqian D, Kerry KR and Wright S (1984) Water masses and circulation in the region of Prydz Bay, Antarctica. *Deep Sea Research Part A: Oceanographic Research Papers* **31**(9), 1121–1147. doi:10.1016/0198-0149(84)90016-5

Sugiyama S, Enomoto H, Fujita S, Fukui K, Nakazawa F and Holmlund P (2010) Dielectric permittivity of snow measured along the route traversed in the Japanese-Swedish Antarctic expedition 2007/08. *Annals of Glaciology* **51**(55), 9–15. doi:10.3189/172756410791392745

Tamura T, Ohshima KI, Fraser AD and Williams GD (2016) Sea ice production variability in Antarctic coastal polynyas. *Journal of Geophysical Research: Oceans* **121**, 2967–2979. doi:10.1002/2015JC011537

Thyssen F (1988) Special aspects of the central part of Filchner-Ronne Ice Shelf, Antarctica. *Annals of Glaciology* **11**, 173–179. doi:10.3189/s0260305500006509

van Wessem JM and 18 others (2018) Modelling the climate and surface mass balance of polar ice sheets using RACMO2 - Part 2: Antarctica (1979-2016). *The Cryosphere* **12**(4), 1479–1498. doi:10.5194/tc-12-1479-2018

Wang Z and 7 others (2023) On the multiscale oceanic heat transports toward the bases of the Antarctic ice shelves. *Ocean-Land-Atmosphere Research* **2**, 0010. doi:10.34133/olar.0010

Williams MJM, Warner RC and Budd WF (2002) Sensitivity of the Amery Ice Shelf, Antarctica, to changes in the climate of the Southern Ocean. *Journal of Climate* **15**(19), 2740–2757. doi:10.1175/1520-0442(2002)015<2740:SOTAIS>2.0.CO;2

Winter A, Steinhage D, Creyts TT, Kleiner T and Eisen O (2019) Age stratigraphy in the East Antarctic Ice Sheet inferred from radio-echo sounding horizons. *Earth System Science Data* **11**(3), 1069–1081. doi:10.5194/essd-11-1069-2019

Wong APS, Bindoff NL and Forbes A (1998) Ocean-ice shelf interaction and possible bottom water formation in Prydz Bay, Antarctica. *Ocean, Ice, and Atmosphere: Interactions at the Antarctic Continental Margin Antarctic Research Series* **75**, 173–187. doi:10.1029/AR075p0173

Yang J and 12 others (2021) Bathymetry beneath the Amery Ice Shelf, East Antarctica, revealed by airborne gravity. *Geophysical Research Letters* **48**(24), e2021GL096215. doi:10.1029/2021GL096215
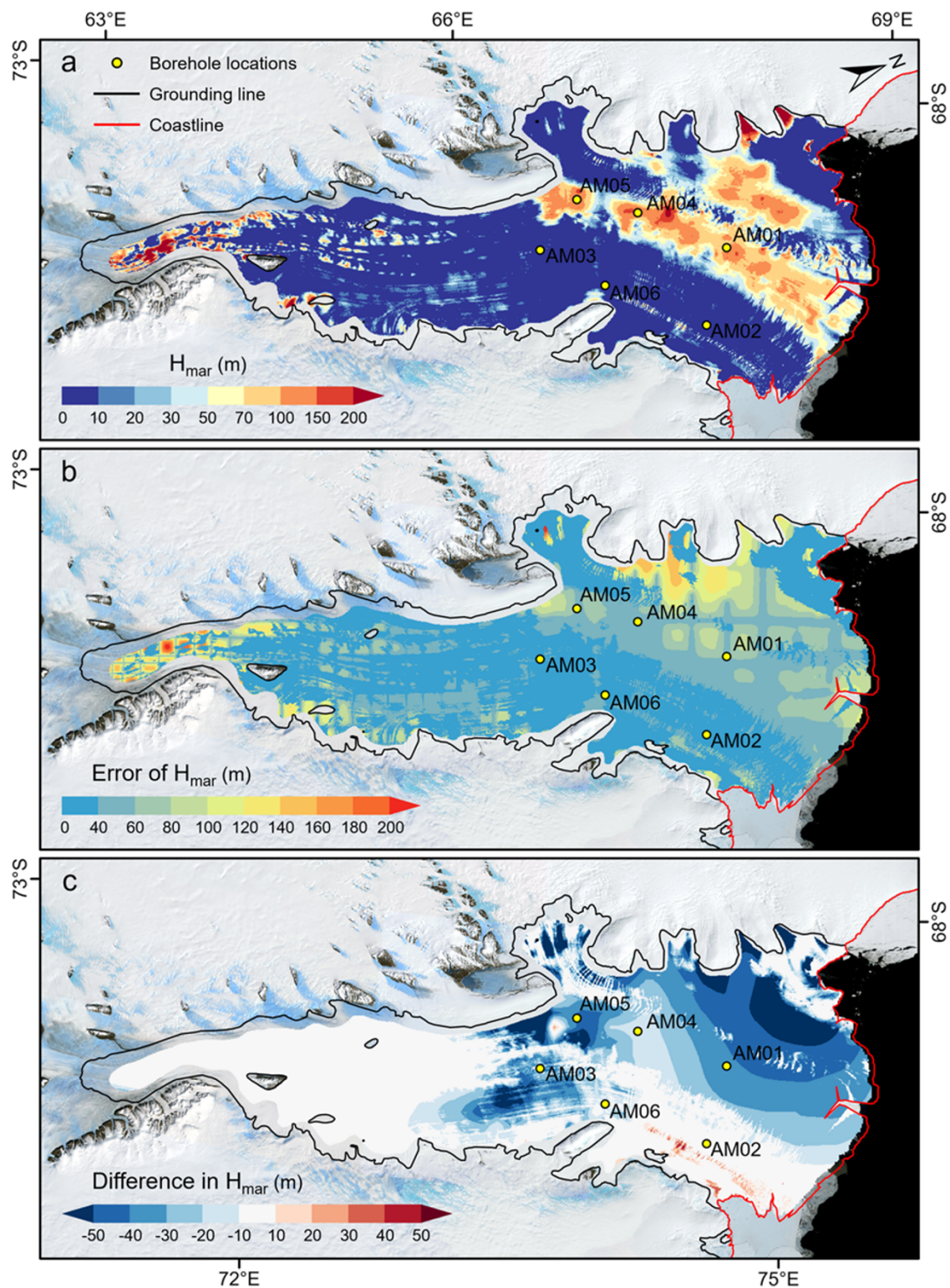
Appendix A

Figure A1. (a) Marine ice thickness beneath the AIS derived from the hydrostatic equilibrium method using RES ice thickness when firn layer is taken into account in the meteoric ice density model. (b) Error map of (a). (c) Difference in marine ice thickness derived from the meteoric ice density model considering firn layer compared to the two-layer model. The yellow circles indicate the locations of six hot water boreholes in the AMISOR project.
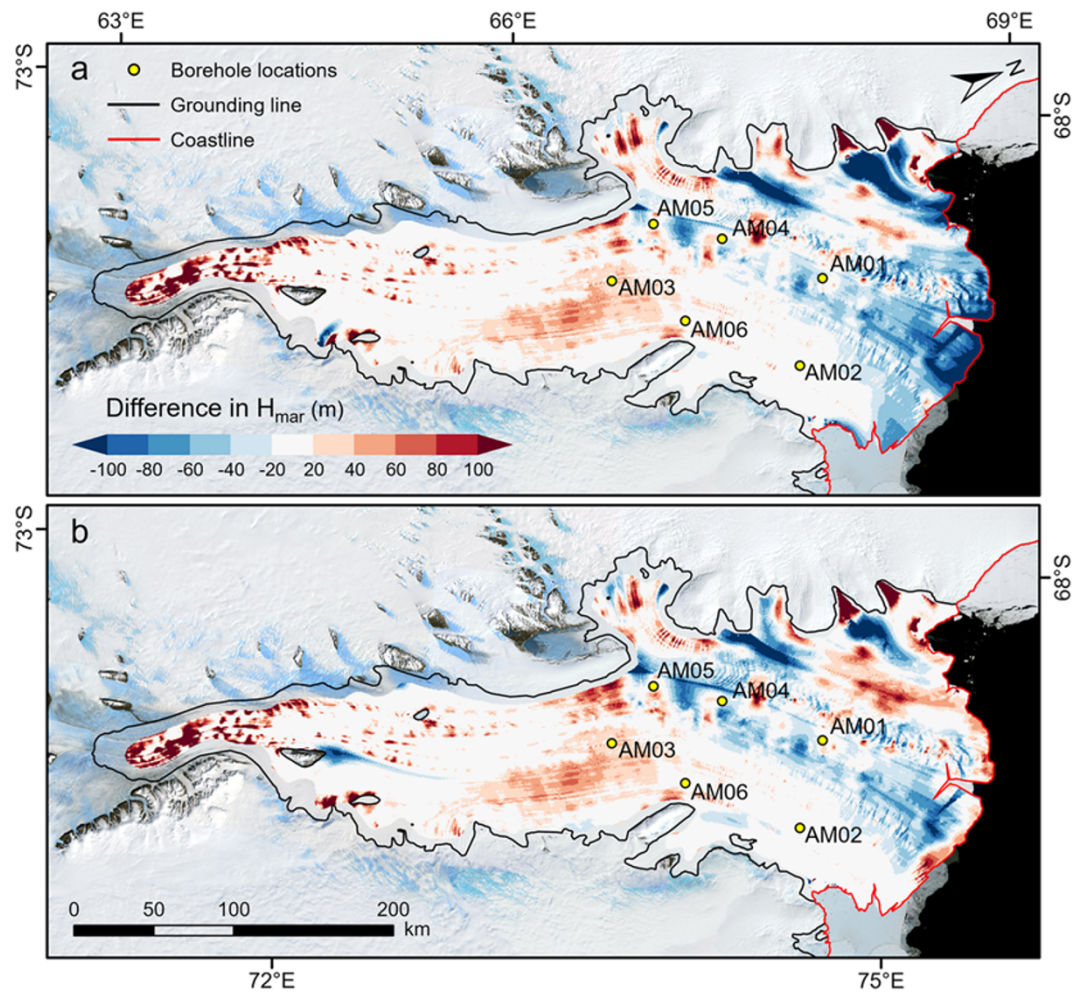
Figure A2. Difference in marine ice thickness derived from the mass conservation method using (a) RES ice thickness and (b) BMA ice thickness compared to the hydrostatic equilibrium method using RES ice thickness. The yellow circles indicate the locations of six hot water boreholes in the AMISOR project.